Solution-Processed MoS$_x$ as an Efficient Anode Buffer Layer in Organic Solar Cells

Xiaodong Li,[†,‡] Wenjun Zhang,[†] Yulei Wu,[†] Chao Min,[†] and Junfeng Fang*[,†]

[†]Ningbo Institute of Materials Technology and Engineering, Chinese Academy of Sciences, Ningbo 315201, China
[‡]University of Chinese Academy of Sciences, Beijing 100049, China

Ⓢ *Supporting Information*

ABSTRACT: We reported a facile solution-processed method to fabricate a MoS$_x$ anode buffer layer through thermal decomposition of $(NH_4)_2MoS_4$. Organic solar cells (OSCs) based on in situ growth MoS$_x$ as the anode buffer layer showed impressive improvements, and the power conversion efficiency was higher than that of conventional PEDOT:PSS-based device. The MoS$_x$ films obtained at different temperatures and the corresponding device performance were systematically studied. The results indicated that both MoS$_3$ and MoS$_2$ were beneficial to the device performance. MoS$_3$ could result in higher V_{oc}, while MoS$_2$ could lead to higher J_{sc}. Our results proved that, apart from MoO$_3$, molybdenum sulfides and Mo^{4+} were also promising candidates for the anode buffer materials in OSCs.
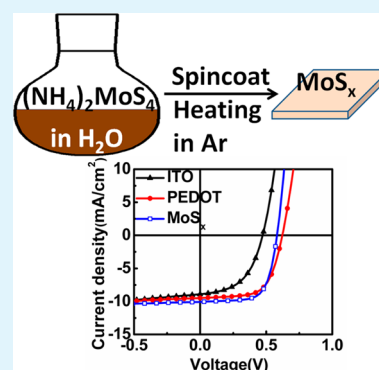
INTRODUCTION

Bulk heterojunction (BHJ) organic solar cells (OSCs) have attracted much attention because of their advantages of low cost, light weight, and flexibility.[1−3] So far, the power conversion efficiency (PCE) of the OSCs has exceeded 9% for the single junction cell,[4] and over 10% has also been reported for a tandem device,[5] which was quite close to commercial requirements. For traditional BHJ OSCs, the active layer was sandwiched between the anode and cathode. To get higher PCE, electrode modification was necessary. Low-work-function metals such as calcium or barium were usually used as the cathode, and poly(3,4-ethylenedioxythiophene):poly-(styrenesulfonate) (PEDOT:PSS) was widely used to improve the work function of the indium−tin oxide (ITO) anode. Although devices based on PEDOT:PSS and an active metal showed excellent device performance, the hygroscopic and acidic nature of PEDOT:PSS as well as the air-sensitive property of the active metal made the OSCs easy to degrade.[6] As a result, severe encapsulation technology was necessary. Recently, various metal oxides/carbonates were applied successfully as electrode modification materials because of their excellent stability. Molybdenum oxides,[7−11] nickel oxides,[12] and vanadium oxides,[13] etc., were developed as the anode buffer layer, and TiO$_2$, ZnO, etc., were used as the cathode buffer layer.[14,15]

Among the reported anode buffer materials, oxides of transition-metal molybdenum have attracted much interest because of their comparable performance with PE-DOT:PSS.[8−11] Both the vacuum-evaporated method and solution-processed routes to realize MoO$_3$ have been

developed. So far, reported results mainly focused on the Mo^{6+} species and their oxides. Systematic analysis indicated that the dominant Mo^{6+} in MoO$_x$ played a major role in interfacial modification and that Mo^{5+} should be alleviated.[9,10] However, there have been limited studies devoted to Mo^{4+} and their sulfides. Recently, MoS$_2$ attracted much attention for its two-dimensional layered structure[16,17] and diverse applications in photocatalysis,[18] electroluminescence,[19] and photolumines-cence[20] and as transistors[21] and light absorbers in solar cells.[22] In 2003, Frey and co-workers prepared a layer-structured MoS$_2$ film through lithium intercalation and exfoliation in aqueous solution.[23] To improve the hole injection in the polymer light-emitting diodes, an oxide layer had to be formed by oxygen plasma treatment. Therefore, molybdenum oxide still played an important role in the device. In 2013, a similar method was used to prepare a MoS$_2$ nanosheet as the anode buffer layer in OSCs.[24] The device showed a moderate PCE of 2.8% based on P3HT and PC$_{61}$BM. After p doping of MoS$_2$, the PCE was improved to 3.4%. However, the MoS$_2$ buffer layer obtained by this chemical exfoliation process usually needs additional treatment, such as oxygen plasma or chemical doping as mentioned above, and the reaction with active butyllithium is not convenient for the operation.

Here, we reported the excellent anode modification function of in situ growth MoS$_x$ without additional treatment for OSCs. MoS$_x$ films were fabricated through simple spin coating of an

ammonium tetrathiomolybdate aqueous solution, followed by thermal treatment in an inert atmosphere. Mo^{4+} was identified to be dominant in the resulting MoS_x films. The PCEs of OSCs with MoS_x as the anode modifier outperformed that of a conventional PEDOT:PSS-based device. By investigating the constituents of MoS_x and their impact on the device performance, we found that both MoS_3 and MoS_2 were beneficial to the device performance. MoS_3 could result in higher V_{oc}, while MoS_2 could lead to higher J_{sc}. Our results proved that, apart from Mo^{6+} and oxides, Mo^{4+} and sulfides were also promising as anode buffer materials for OSCs.

$(NH_4)_2MoS_4$ was widely reported in the literature to prepare MoS_2 for catalytic and semiconducting applications.[16,25,26] When heated at 150−200 °C in an inert atmosphere, $(NH_4)_2MoS_4$ can decompose to MoS_3. Furthermore, when the temperature was increased to 300 °C, conversion from MoS_3 to MoS_2 happened. At even higher temperature (400−1000 °C), specific two-dimensional or highly crystalline MoS_2 can be achieved. For conventional OSCs, an ITO-coated glass substrate was used as the anode in general, but an ITO substrate cannot endure high-temperature treatment. Therefore, we mainly focused on the study of OSCs with the MoS_x films obtained at relatively low temperature ($\leqslant$400 °C). For device characterization, ITO/MoS_x was used as the anode, and a poly(3-hexylthiophene) and [6,6]phenyl-C61-butyric acid methyl ester (P3HT:$PC_{61}BM$) blend was chosen as the bulk photoactive layer. Devices based on ITO/PEDOT:PSS and bare ITO as the anode were also fabricated in the same conditions for comparison. The chemical structure and device configuration are shown in Figure 1. Through optimization, the device with MoS_x showed a high PCE of 3.90%, which was even better than that of a PEDOT:PSS-based device (3.64%).
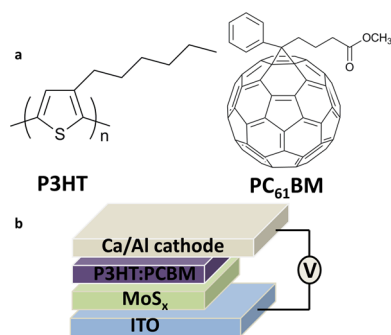

Figure 1. (a) Molecular structures of P3HT and $PC_{61}BM$. (b) Device configuration used in our work.

■ EXPERIMENTAL SECTION

Preparation of a MoS_x Precursor Solution. $(NH_4)_2MoS_4$ was dissolved in deionized water with a concentration of 10 mg/mL at 60 °C in an inert atmosphere. The solution was then filtered through a 0.22 μm poly(tetrafluoroethylene) filter.

Device Fabrication. The ITO glass was cleaned by sequential ultrasonic treatment in detergent, deionized water, acetone, and isopropyl alcohol for 15 min each. Then, the precleaned ITO glass was moved into an ultraviolet (UV) chamber for UV−ozone treatment for 20 min. The precursor film (about 20 nm) was deposited on ITO through spin coating of a $(NH_4)_2MoS_4$ aqueous solution at 1000 rpm for 90 s. Then, the film was heated in a glovebox (argon atmosphere, O_2 < 0.1

ppm, H_2O < 0.1 ppm). PEDOT:PSS (Clevios 4083) was spin-coated onto ITO at 4000 rpm for 60 s to form a 35 nm film and dried at 150 °C for 20 min in air. At last, the photoactive materials were spin-coated in a glovebox at 600 rpm for 60 s (about 220 nm) with a 1,2-dichlorobenzene solution of P3HT:$PC_{61}BM$ [1:1 (w/w); polymer concentration of 20 mg/mL]. Then, they were covered in glass Petri dishes for solvent annealing and preannealed at 110 °C for 10 min. Finally, the substrates were transferred into a vacuum chamber (10^{-6} mbar), and 20 nm of calcium (deposition rate of 0.3 Å/s) and 100 nm of aluminum (deposition rate of 1.1 Å/s) were thermally deposited onto the photoactive layer. The effective area of the device was 4 mm².

■ RESULTS AND DISCUSSION

Figure 2 shows the current density versus voltage curves ($I−V$) of OSCs under an illumination of AM 1.5G with an irradiation
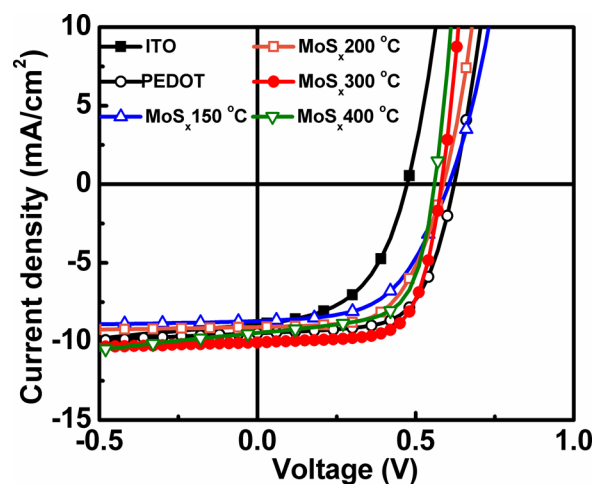

Figure 2. Current density−voltage curves ($I−V$) of OSCs with bare ITO, PEDOT:PSS, and MoS_x at 150, 200, 300, and 400 °C as the anode buffer layer under an illumination of AM 1.5G with an irradiation of 100 mW/cm².

of 100 mW/cm². The device with bare ITO showed very poor performance with an open-circuit voltage (V_{oc}) of 0.472 V, a short-circuit current density (J_{sc}) of 8.91 mA/cm², and a fill factor (FF) of 51%, resulting in a PCE of 2.14%. The poor performance could be ascribed to the high work function of ITO and the direct contact between ITO and $PC_{61}BM$, which led to a large leakage current and series resistance. Compared with those of a device based on bare ITO, the PCEs of devices with MoS_x as the buffer layer were improved significantly. However, it was obvious that the MoS_x buffer layers obtained at different heating temperatures showed different improvements. The device with MoS_x processed at 150 °C showed an enhanced PCE of 2.91%, mainly because of the much improved V_{oc} (from 0.472 to 0.605 V). The PCE of a device with MoS_x obtained at 200 °C was 3.15%. The improvement of the PCE was mainly due to both increasing V_{oc} (from 0.472 to 0.590 V) and FF (from 51% to 59%). For the device with MoS_x obtained at 300 °C, device parameters including V_{oc}, J_{sc}, and FF were all significantly improved, and as a result, the PCE was increased to 3.90%. The performance was even better than that of a conventional PEDOT:PSS-based device fabricated in the same conditions (3.64%). Compared with the conventional device, the improvements mainly came from the enhanced J_{sc} of 9.96

mA/cm^2 and FF of 67%, despite the slightly lower V_{oc} of 0.581 V, while when the temperature was further increased to 400 °C, the device performance was decreased to 3.57% because V_{oc} and J_{sc} decreased ∼3% and ∼6%, respectively. The results are all summarized in Table 1 (specific statistical analysis can be

Table 1. Specific Device Parameters of OSCs Based on P3HT and PC$_{61}$BM with Bare ITO, PEDOT:PSS, and MoS$_x$ at 150, 200, 300, and 400 °C as the Anode Buffer Layer[a]

HTL	V_{oc} (V)	J_{sc} (mA/cm^2)	FF (%)	PCE (%)	R_s (Ω cm^2)	R_{sh} (Ω cm^2)
bare ITO	0.472	8.91	51	2.14	11.96	505
ITO/PEDOT	0.611	9.47	62	3.64	9.18	1523
ITO/MoS$_x$ at 150 °C	0.605	8.66	56	2.91	16.96	1633
ITO/MoS$_x$ at 200 °C	0.590	9.02	59	3.15	13.54	1503
ITO/MoS$_x$ at 300 °C	0.581	9.96	67	3.90	6.50	1308
ITO/MoS$_x$ at 400 °C	0.566	9.42	67	3.57	7.36	1022

[a]R_s is the series resistance, and R_{sh} is the shunt resistance. (The data of PEDOT and MoS$_x$ at 300 °C were based on 18 separated devices. The others were based on at least 8 devices.)

seen in the Supporting Information, SI). The results presented here obviously proved that, apart from MoO$_3$, molybdenum sulfides were also promising candidates for anode buffer materials in OSCs.

The Raman spectra of MoS$_x$ obtained at different temperature are shown in Figure 3. The E$^1_{2g}$ mode at ∼380 cm^{-1} and the A$_{1g}$ mode at ∼404 cm^{-1} indicated the planar vibration and out-of-plane vibration of sulfides in MoS$_2$, respectively.[27] MoS$_3$ showed broad peaks around 320 and 520 cm^{-1}.[28] From the Raman spectra, we can see that the characteristic peaks of MoS$_2$ were not obvious at 150 °C. This observation was not unexpected because MoS$_3$ was dominated in this stage.[26] However, when the temperature was increased to 200 °C, a weak peak at 404 cm^{-1} can be noted, indicating the formation of MoS$_2$ in the film,[16] while at 300 °C, peaks around 380 and 404 cm^{-1} became stronger and better defined, implying an increasing amount of MoS$_2$ formed. At last, when the temperature was further increased to 400 °C, peaks of MoS$_3$ at 320 and 520 cm^{-1} disappeared, indicating that remnant MoS$_3$ converted to MoS$_2$ completely.

To further understand the changes during thermal treatments, we studied the chemical states of the MoS$_x$ film through X-ray photoelectron spectroscopy (XPS), with the binding energy of the C 1s peak being fixed at 284.8 eV. The XPS of S 2p core-level spectra are shown in Figure 4. We found noticeable changes in the peak shape with an increase in the temperature. The spectra at 150 and 200 °C showed a peak at 163.2 eV, which suggested that decomposition of (NH$_4$)$_2$MoS$_4$ happened. The peak at 161.7 eV was from the residual (NH$_4$)$_2$MoS$_4$,[29] and this was confirmed further by the XPS spectra of Mo 3d (Figure S2 in the SI). For the spectrum at 300 °C, the spin−orbit splitting of the S 2p orbital became clear, as evidenced by the fact that the S 2p$_{3/2}$ peak at 162.3 eV appeared strongly. At 400 °C, the S 2p orbital split completely into two peaks, centered at 163.6 and 162.4 eV, respectively, which corresponded to S 2p$_{1/2}$ and S 2p$_{3/2}$ orbitals of divalent sulfide ions (S$^{2−}$).[16,30] The XPS spectra of Mo 3d (peaks at 229.3 and 232.5 eV; Figure S2 in the SI) were also consistent
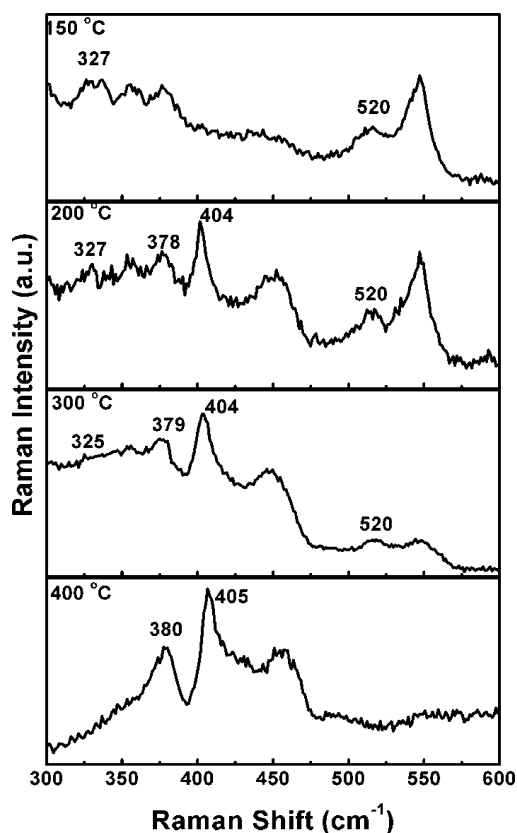

Figure 3. Raman spectra of the MoS$_x$ film obtained on ITO at 150, 200, 300, and 400 °C. The peaks around 380 and 404 cm^{-1} are characteristic peaks of MoS$_2$.
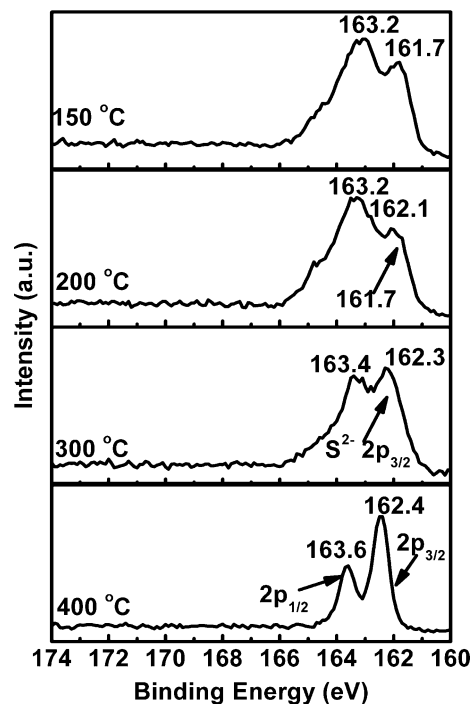

Figure 4. XPS measurement of the S 2p orbital in the MoS$_x$ film on ITO obtained at 150, 200, 300, and 400 °C. It is clear that, at 150 and 200 °C, the broad peak at 163.2 eV of the S 2p orbital was characteristic for MoS$_3$. At higher temperatures of 300 and 400 °C, the S 2p peaks started to split and became similar to the peaks of MoS$_2$.

with the previously reported results about MoS_2.[16] Furthermore, we found that the S/Mo atomic ratio changed as the heating temperature increased. The calculated S/Mo ratios were 3.0, 2.85, 2.33, and 1.80 for the MoS_x film at 150, 200, 300, and 400 °C, respectively. This trend indicated that, with increasing temperature, MoS_3 in MoS_x films slowly decreased and finally converted to MoS_2 at 400 °C completely. From the results mentioned above, we could find that, when MoS_3 was dominated in the MoS_x film (at 150 and 200 °C), the device showed a relatively higher V_{oc} but a lower J_{sc}. With increased processing temperature (300 °C), an increasing amount of MoS_2 formed. V_{oc} decreased to 0.581 V, while J_{sc} increased to 9.96 mA/cm^2. Finally, when at 400 °C MoS_2 was completely formed, V_{oc} continued to rapidly decrease to 0.566 V and J_{sc} slightly decreased to 9.42 mA/cm^2. However, J_{sc} was still higher than those of 150 and 200 °C. Thus, we can conclude that the J_{sc} values of devices were improved with increased MoS_2, but V_{oc} was obviously decreased. When the components of MoS_3 and MoS_2 reached a relatively appropriate balance (300 °C), both V_{oc} and J_{sc} were improved and the highest PCE of 3.90% was achieved. In addition, we noted that no matter whether MoS_3 or MoS_2 dominated in the MoS_x film, the FF was improved effectively compared to that of the bare ITO device. The FF values of devices with the MoS_x film processed at 300 and 400 °C were even higher than that of the PEDOT:PSS-based device, which was consistent with the decreased series resistance.

We also studied ultraviolet photoelectron spectroscopy (UPS; Figure S6 in the SI) and calculated the energy-level structures of MoS_x (Figure 5) obtained at different temper-
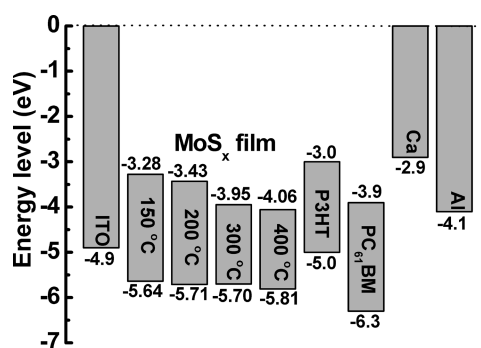

Figure 6. (a) AFM image with tapping mode of PEDOT:PSS on ITO. (b) Corresponding 3D image of PEDOT:PSS. (c) AFM image of the MoS_x film obtained at 300 °C on ITO. (d) 3D image of MoS_x. The scan size was 5 μm × 5μm.

Figure 5. Energy-level diagram of the corresponding device based on MoS_x obtained at 150, 200, 300, and 400 °C.

atures by combining with the absorption spectrum (Figure S3 in the SI). The results (Table S1 in the SI) indicated that the valence band (VB) of MoS_x gradually moved downward with increasing temperature (from 5.64 eV at 150 °C to 5.81 eV at 400 °C). The conduction band (CB) shifted from 3.28 eV at 150 °C to 4.06 eV at 400 °C. The low-lying VB of MoS_x obtained at different temperatures indicated excellent hole extraction and led to improvements of the device performance. Although the carrier collection of MoS_x processed at high temperature was improved, the chance of recombination at the interface was also increased because of the lower CB, which could be a reason for the lower V_{oc} of the device with MoS_x processed at high temperature.

Figure 6 shows atomic force microscopy (AFM) images of PEDOT:PSS and MoS_x on ITO. The PEDOT:PSS on ITO exhibited a rather smooth surface with a root-mean-square (RMS) roughness of only 1.74 nm, while the MoS_x film
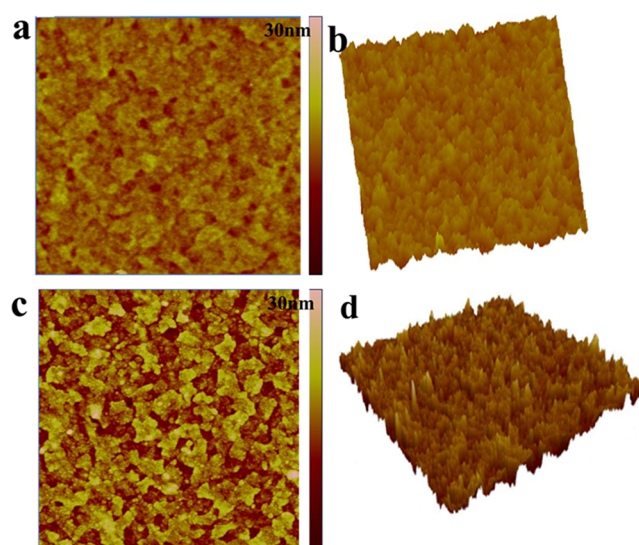
processed at 300 °C showed a larger RMS roughness (3.89 nm). The slightly rough surface may enhance the contact area between the anode and P3HT, thus facilitating the hole collection efficiency. Finally, the external quantum efficiency (EQE) and transmittance spectrum of the MoS_x film were also studied (Figure S4 in the SI). Over the wavelength examined (from 400 to 1000 nm), the MoS_x film showed good transmittance over 70%, while compared with bare ITO, the MoS_x film processed at 300 °C showed an apparently low transmittance around 430-nm wavelength, agreeing with the MoS_2 absorption peak at 430 nm (Figure S3 in the SI).[23] Compared to bare ITO or the PEDOT:PSS-based device, an additional peak at about 430 nm appeared obviously in the EQE measurement, which may be caused by the absorption peak of MoS_2 in the MoS_x film. However, in the range from 450 to 550 nm, the MoS_x-based device showed slightly lower EQE. As a result, the J_{sc} enhancement was limited for the MoS_x-based device.

CONCLUSION

In conclusion, we proposed a facile method to fabricate the MoS_x film. OSCs based on in situ growth of the MoS_x film as the anode buffer layer showed impressive improvements, and the PCE was even better than that of a conventional PEDOT:PSS-based device. The MoS_x film was systematically examined by Raman spectroscopy, XPS, UPS, and AFM. The results indicated that both MoS_3 and MoS_2 were beneficial to the device performance. MoS_2 could lead to higher J_{sc} because of improved hole extraction and light absorption, but V_{oc} decreased because of the lower CB and, hence, resulted in recombination at the interface. When MoS_3 and MoS_2 reached the balance, the highest PCE of 3.90% was achieved, which was even higher than that of a conventional PEDOT:PSS-based device (3.64%). Our results proved that, apart from MoO_3, molybdenum sulfides and Mo^{4+} were also promising candidates for anode buffer materials in OSCs.

8826

dx.doi.org/10.1021/am402105d | ACS Appl. Mater. Interfaces 2013, 5, 8823–8827

■ ASSOCIATED CONTENT

ⓢ Supporting Information

$I-V$ curves of OSCs measured in dark conditions, XPS of a Mo 3d orbital at 150, 200, 300, and 400 °C, UV−vis spectra of the MoS_x film on quartz, EQE measurement of a device with different buffer layers and transmittance spectra of bare ITO, ITO/PEDOT:PSS, and ITO/MoS_x, SEM image of the MoS_x film obtained at 300 °C, UPS of the MoS_x film on ITO, statistical analysis of the device performance based on MoS_x at 300 °C and PEDOT, and summary of the energy level for MoS_x. This material is available free of charge via the Internet at http://pubs.acs.org.

■ AUTHOR INFORMATION

Corresponding Author

*E-mail: fangjf@nimte.ac.cn.

Notes

The authors declare no competing financial interest.

■ ACKNOWLEDGMENTS

■ REFERENCES

(1) Yu, G.; Gao, J.; Hummelen, J.; Wudl, F.; Heeger, A. J. *Science* **1995**, 1789−1791.

(2) Li, G.; Zhu, R.; Yang, Y. *Nat. Photon.* **2012**, *6*, 153−161.

(3) Gunes, S.; Neugebauer, H.; Sariciftci, N. S. *Chem. Rev.* **2007**, *107*, 1324−1338.

(4) He, Z.; Zhong, C.; Su, S.; Xu, M.; Wu, H.; Cao, Y. *Nat. Photon.* **2012**, *6*, 591−595.

(5) You, J.; Dou, L.; Yoshimura, K.; Kato, T.; Ohya, K.; Moriarty, T.; Emery, K.; Chen, C.-C.; Gao, J.; Li, G. *Nat. Commun.* **2013**, *4*, 1446−1456.

(6) Yip, H.-L.; Jen, A. K.-Y. *Energy Environ. Sci.* **2012**, *5*, 5994−6011.

(7) Fu, Q.; Chen, J.; Shi, C.; Ma, D. *ACS Appl. Mater. Interfaces* **2013**, DOI: 10.1021/am 4007319.

(8) Murase, S.; Yang, Y. *Adv. Mater.* **2012**, *24*, 2459−2462.

(9) Jasieniak, J. J.; Seifter, J.; Jo, J.; Mates, T.; Heeger, A. J. *Adv. Funct. Mater.* **2012**, *22*, 2594−2605.

(10) Girotto, C.; Voroshazi, E.; Cheyns, D.; Heremans, P.; Rand, B. P. *ACS Appl. Mater. Interfaces* **2011**, *3*, 3244−3247.

(11) Wong, K. H.; Ananthanarayanan, K.; Luther, J.; Balaya, P. *J. Phys. Chem. C* **2012**, *116*, 16346−16351.

(12) Tan, Z. a.; Zhang, W.; Qian, D.; Cui, C.; Xu, Q.; Li, L.; Li, S.; Li, Y. *Phys. Chem. Chem. Phys.* **2012**, *14*, 14217−14223.

(13) Zilberberg, K.; Trost, S.; Meyer, J.; Kahn, A.; Behrendt, A.; Lützenkirchen-Hecht, D.; Frahm, R.; Riedl, T. *Adv. Funct. Mater.* **2011**, *21*, 4776−4783.

(14) Park, S. H.; Roy, A.; Beaupré, S.; Cho, S.; Coates, N.; Moon, J. S.; Moses, D.; Leclerc, M.; Lee, K.; Heeger, A. J. *Nat. Photon.* **2009**, *3*, 297−302.

(15) Sun, Y.; Seo, J. H.; Takacs, C. J.; Seifter, J.; Heeger, A. J. *Adv. Mater.* **2011**, *23*, 1679−1683.

(16) Liu, K.-K.; Zhang, W.; Lee, Y.-H.; Lin, Y.-C.; Chang, M.-T.; Su, C.-Y.; Chang, C.-S.; Li, H.; Shi, Y.; Zhang, H. *Nano Lett.* **2012**, *12*, 1538−1544.

(17) Chou, S. S.; De, M.; Kim, J.; Byun, S.; Dykstra, C.; Yu, J.; Huang, J.; Dravid, V. P. *J. Am. Chem. Soc.* **2013**, *135*, 4584−4587.

(18) Xiang, Q.; Yu, J.; Jaroniec, M. *J. Am. Chem. Soc.* **2012**, *134*, 6575−6578.

(19) Sundaram, R. S.; Engel, M.; Lombardo, A.; Krupke, R.; Ferrari, A. C.; Avouris, P.; Steiner, M. *Nano Lett.* **2013**, *13*, 1416−1421.

(20) Eda, G.; Yamaguchi, H.; Voiry, D.; Fujita, T.; Chen, M.; Chhowalla, M. *Nano Lett.* **2011**, *11*, 5111−5116.

(21) Radisavljevic, B.; Radenovic, A.; Brivio, J.; Giacometti, V.; Kis, A. *Nat. Nanotechnol.* **2011**, *6*, 147−150.

(22) Shanmugam, M.; Bansal, T.; Durcan, C. A.; Yu, B. *Appl. Phys. Lett.* **2012**, *100*, 153901-1−153901-4.

(23) Frey, G. L.; Reynolds, K. J.; Friend, R. H.; Cohen, H.; Feldman, Y. *J. Am. Chem. Soc.* **2003**, *125*, 5998−6007.

(24) Yun, J.-M.; Noh, Y.-J.; Yeo, J.-S.; Go, Y.-J.; Na, S.-I.; Jeong, H.-G.; Kim, J.; Lee, S.; Kim, S.-S.; Koo, H. Y. *J. Mater. Chem. C* **2013**, *1*, 3777−3783.

(25) Zelenski, C. M.; Dorhout, P. K. *J. Am. Chem. Soc.* **1998**, *120*, 734−742.

(26) Walton, R. I.; Dent, A. J.; Hibble, S. *Chem. Mater.* **1998**, *10*, 3737−3745.

(27) Zhan, Y.; Liu, Z.; Najmaei, S.; Ajayan, P. M.; Lou, J. *Small* **2012**, *8*, 966−971.

(28) Chang, C.; Chan, S. *J. Catal.* **1981**, *72*, 139−148.

(29) Ye, X.; Hou, H.; Xin, X.; Hammer, C. *Appl. Surf. Sci.* **1995**, *89*, 151−157.

(30) Benck, J. D.; Chen, Z.; Kuritzky, L. Y.; Forman, A. J.; Jaramillo, T. F. *ACS Catal.* **2012**, *2*, 1916−1923.

8827

dx.doi.org/10.1021/am402105d | *ACS Appl. Mater. Interfaces* 2013, 5, 8823−8827